A Cloud and Cloud Shadow Detection Method Based on Fuzzy c-Means Algorithm

Ping Bo, Su Fenzhen, and Meng Yunshan

***Abstract*—Cloud and cloud shadow detection is an important preprocess before using satellite images for different applications. It can be considered as a classification process, in which the objective pixels are partitioned into cloud/cloud shadow or non-cloud/non-cloud shadow classes. However, some cloud pixels, especially the thin cloud pixels, can be considered as a mixture of reflectances of clouds and land objects. In fuzzy clustering, the data points can belong to two or more clusters; hence, fuzzy clustering may better characterize the status of one given pixel belonging to clouds or non-clouds. The fuzzy c-means method (FCM), one typical fuzzy clustering method, was utilized in this study for cloud and cloud shadow detection. In addition, the "flood-fill" morphological transformation may misclassify some clear-sky areas surrounded by clouds as cloud shadows as a whole, so a modified cloud shadow index calculation was proposed. Moreover, a cloud and cloud shadow spatial matching strategy based on the projection direction and spatial coexistence was used to exclude some pseudo cloud shadows. Fewer predefined parameters and spectral bands are needed is one characteristic of the proposed method. In this study, 41 scenes including 27 Landsat ETM+ images in eight latitude zones and 14 Landsat OLI images comprising seven land cover types, including barren, forest, grass, shrubland, urban, water, and wetlands areas, with percentages of cloud cover from 4.99% to 97.63%, were utilized to confirm the validity of the FCM. The detected results demonstrate that the thick and thin clouds along with their associated cloud shadows can be precisely extracted by using the FCM. Compared with the function of mask (Fmask) method, the FCM has relatively lower producer agreement rates, but it misclassifies as clouds fewer clear-sky pixels; compared with the support vector machine (SVM) method, the FCM can achieve better cloud detection accuracy. The results demonstrate that the FCM can attain a better balance between cloud pixel detection and non-cloud pixel exclusion.**

***Index Terms*—Cloud and cloud shadow detection, fuzzy c-means algorithm, multiple features, multispectral sensors.**

I. Introduction

THE spectral bands of optical sensors are commonly influenced by clouds and cloud shadows [1]–[4]. In light of the International Satellite Cloud Climatology Project-Flux Data (ISCCP-FD), the global annual average cloud cover is close to 66% [5]. The surface of the Earth, when covered by clouds and cloud shadows, cannot be correctly presented in the satellite images; this could, in turn, affect many types of studies, such as those on atmospheric correction, land cover classification and change detection, and feature extraction [2], [6]. Hence, cloud and cloud shadow detection is an essential preprocess before using satellite images for different applications.

During the last two decades, many automated methods for screening clouds and cloud shadows have been developed and widely applied to various satellite images. Generally, existing methods for cloud and cloud shadow detection can be roughly grouped into two main classes: multi-temporal methods and single-image methods. Multi-temporal methods [7]–[13] mainly use the temporal continuity in time series as a principal criterion for enhancing the cloud detection accuracy. However, the temporal discontinuity caused by the land cover change can affect the effectiveness of the multi-temporal methods; meanwhile, a cloud-free reference image may be not available directly or be difficult to generate. Hence, single-image methods are more popular, to some extent, because of the reduced requirement for input data [6], [11], [14]–[15]. In this study, we focus on single-image methods.

Spectral analysis methods have been widely used to separate clouds from clear-sky pixels. The automatic cloud cover assessment (ACCA) algorithm [1] has been utilized officially for cloud cover assessment of Landsat-7 imagery and been introduced in the Landsat-7 Science Data User's Handbook [16]. The ACCA algorithm has 2 individual tests and more than 30 parameters to separate clouds and snow from clear observations. The haze optimized transformation (HOT) method [17] utilized the distances to the "clear-sky" line generated from regression of DNs or reflectance values from clear-sky pixels in the blue-red spectral space to separate clouds and non-clouds pixels. However, it could not effectively eliminate the influences from bright clear-sky ground objects, such as rocks and snow [2]. Chen et al. [18] proposed an iterative HOT (IHOT) method to improve haze detection under the help of a cloud-free image. Later, Chen *et al.* [19] used the IHOT method and the cloud removal of cloud trajectory (IHOT-Trajectory) to rectify cloud contamination. Zhu and Woodcock [2] proposed the function of mask (Fmask) method to detect clouds, snow, and cloud shadows in Landsat images. There are more than 20 predefined and adaptive thresholds in the Fmask method. After that, some modified versions of Fmask method have been proposed to

Manuscript received December 24, 2019; revised February 18, 2020 and March 20, 2020; accepted April 11, 2020. Date of publication April 22, 2020; date of current version May 5, 2020. This work was supported in part by the Natural Science Foundation of Tianjin under Grant 18JCQNJC08900 and in part by State Key Laboratory of Resources and Environmental Information System. *(Corresponding author: Ping Bo.)*

Ping Bo is with the Institute of Surface-Earth System Science, Tianjin University, Tianjin 300072, China (e-mail: pingbo@tju.edu.cn).

Su Fenzhen is with LREIS, Institute of Geographic Sciences and Natural Resources Research, University of the Chinese Academy of Sciences, Beijing 100101, China (e-mail: sufz@lreis.ac.cn).

Meng Yunshan is with the National Marine Data and Information Service, Tianjin 300171, China (e-mail: mengys@lreis.ac.cn).

Digital Object Identifier 10.1109/JSTARS.2020.2987844

This work is licensed under a Creative Commons Attribution 4.0 License. For more information, see https://creativecommons.org/licenses/by/4.0/

enhance the detection accuracy [20]–[22]. Li et al. [6] used a multi-feature combined (MFC) method to mask the clouds and cloud shadows of Gaofen-1 wide field of view (GF-1 WFV) imagery. After obtaining an initial cloud mask by employing three spectral tests, the guided filter was used to detect the thin clouds around the cloud edges; moreover, the geometric and texture characteristics were then incorporated to lessen the commission errors. An improved cloud and cloud shadow matching method was also used in the MFC cloud shadow detection step. Sun et al. [23] presented a cloud detection algorithm-generating (CDAG) method for satellite images in the visible to short-wave infrared (SWIR) bands. Zhai et al. [24] utilized the spectral indices (CSD-SI) to detect the clouds and cloud shadows for diverse multi/hyperspectral satellite images. Generally, the thresholds are decisive parameters in spectral analysis methods; however, setting these thresholds seems to be subjective and numerous experiments are needed before the best thresholds are acquired. In addition, some methods cannot be used directly for other satellite images. For example, the Fmask method uses the visible and infrared bands of Landsat images to mask clouds, but it will fail to screen clouds for satellite images without thermal infrared bands, such as the GF-1 WFV and HJ-1A/B CCD imagery of China. Hence, to improve the applicability of the proposed method, only visible and NIR bands were used in this study, even though the involvement of more appropriate bands, such as the thermal and cirrus bands of Landsat 8, can enhance the accuracy of cloud detection.

Recently, machine learning methods, such as neural network-based methods [25]–[26], Markov random field-based methods [27], support vector machine (SVM) [28]–[32] or k-means [13] classification methods have become more and more popular in cloud detection. For most machine learning methods, an appropriate training dataset which is, to some extent, subjective and time-consuming to select is indispensable for constructing the classifier. Moreover, some pixels, such as the thin clouds surrounding thick opaque clouds, can be deemed as a mixture of reflectances of clouds and land objects, so certain membership grades that represent the degree to which they belong to cloud or non-cloud clusters may better characterize the statuses of these pixels. Therefore, we used a fuzzy c-mean clustering method (FCM), one typical fuzzy clustering method, to identify the clouds and cloud shadows in this study.

The FCM method was also used in cloud shadow detection. Because cloud shadows cannot exist without clouds, a spatial matching method is often applied to refine the initial cloud shadow pixels. The matching methods can be roughly grouped into two classes. The first class is based on the projection law [2], [6]. By obtaining the solar and sensor azimuth and zenith angles and the height of the cloud, the cloud shadow location corresponding to one given cloud can be predicted based on a geometric relationship. However, although the first four factors can be acquired from the metadata files, the height of the cloud is commonly unknown. Hence, in practice, the height of cloud is usually set from 200 to 12 000 m and the cloud shadow location is calculated iteratively based on the predefined height until it meets a shape similarity criterion. Actually, different clouds may have different heights; thus, the iteration above should be applied for each cloud object. Therefore, the computational cost may be fairly high. The second class considers that if some cloud pixels can be found in the neighborhood of cloud shadows, the cloud shadows can be regarded as real; otherwise, they are not and can be removed. Methods in this category can acquire cloud shadow masks in a short time, but their accuracy may be affected by factors including local window size setting, and searching direction. In this study, we combined these two types of matching schemes, i.e., the former was used to determine the searching direction and the latter was used to find the cloud shadow pixels. In addition, we also proposed a new cloud shadow detection strategy to enhance the detection accuracy of the regions surrounded by clouds.

TABLE I
CLOUD AND CLOUD SHADOW MASKING DATASETS AND THEIR CHARACTERISTICS

Name	Scenes	Spatial resolution	Sensor	Cloud	Thin Cloud	Cloud shadow
L7	27	30m	ETM+	Yes	Yes	Some
L8	14	30m	OLI	Yes	Yes	Some

II. EXPERIMENTAL DATA

Two existing cloud and cloud shadow masking datasets called "L7 Irish" and "L8 Biome" were used in this study to validate the effectiveness of the FCM (Table I). The "L7 Irish" images, which were chosen by Irish et al. [1] and digitized by Scaramuzza et al. [34], were divided into nine subsets according to their different spatial locations; the "L8 Biome" images, which were digitized by Foga et al. [35], were divided equally into eight groups according to different land cover types. These masks all contain cloud and thin cloud classes, and some of them contain a cloud shadow class. All the "L7 Irish" and "L8 Biome" masks can be freely downloaded online [36]–[37].

In this study, we selected 27 "L7 Irish" masks and 14 "L8 Biome" masks from all the subsets of the two validation datasets. The percentages of cloud cover range from 4.99% to 97.63% in this study. The L7 Irish scenes were acquired from January to December 2001 in eight latitude zones, and the L8 Biome scenes were obtained from June 2013 to August 2014 and covered seven land cover types, including barren, forest, grass, shrubland, urban, water, and wetlands areas. The digital number (DN) values of all input data were first converted to top of atmosphere (TOA) reflectance for all experimental bands, i.e., blue, green, red, and NIR. Converting the DN values into the TOA reflectance can reduce the between-scene variability [6]. To improve the applicability of the proposed method, only visible and NIR bands were involved in this study (explained in the Introduction part). We acknowledge that only these bands cannot perfectly detect all clouds, especially for surfaces covered by snow or bright buildings. Hence, some images with obvious snow or bright buildings were excluded. It seems to be unfair to compare the proposed method to Fmask (used as a reference method) based on these images, because Fmask was fulfilled in the ENVI software and operated by using all Landsat bands. Also, the proposed method can be deemed as a classification

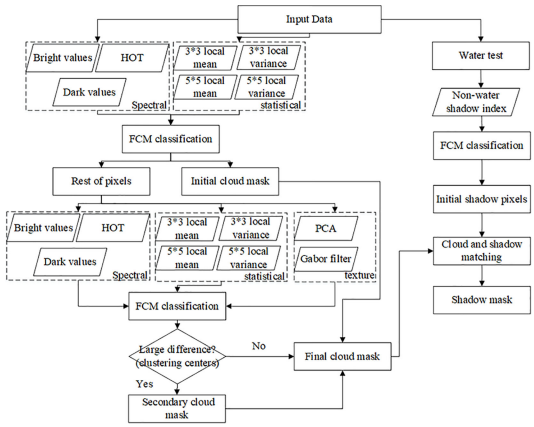

Fig. 1. Flowchart of the fuzzy c-means cloud and cloud shadow detection.

issue, so it may be not suitable for some images with extreme high (such as 98%) or low (0% or 1%) percentages of clouds, and these masks were excluded.

III. Methodology

There are four main steps in FCM cloud detection and three main steps in cloud shadow detection. The four main steps of cloud detection are as follows: (1) three cloud features including spectral, statistical and texture features are first computed by using the blue, green, red and NIR bands to highlight cloud pixels; (2) the spectral and statistical features are used for the initial cloud detection by using the FCM; (3) all cloud features of the pixels belonging to the non-cloud class after the first FCM classification are then employed for the secondary cloud detection by operating the FCM again; (4) the cloud pixels obtained from the secondary cloud detection are verified to determine whether the secondary cloud detection is necessary. If the secondary cloud detection is valid, then the cloud pixels from the initial and secondary cloud detection can generate the final cloud mask; otherwise, only the cloud pixels from the initial cloud detection are deemed as clouds.

The three main steps of cloud shadow detection are as follows: (1) the water pixels are separated by using the water test and the NIR band is used for calculating the cloud shadow index for non-water pixels; (2) the initial cloud shadow pixels can be acquired by applying the FCM to the cloud shadow index; (3) a rapid cloud and cloud shadow matching method is applied to acquire the final cloud shadow pixels. The flowchart of the FCM is shown in Fig. 1.

A. Fuzzy c-Means Method (FCM)

The FCM developed by Dunn [38] is a typical fuzzy clustering method that allows data points to belong to more than one cluster. Its aim is to minimize the objective function which can be calculated using Eq. 1 by optimizing iteratively membership μ_{ij} and cluster centers c_j obtained by (2):

$$J_m = \sum_{a=1}^{n}\sum_{b=1}^{c} \mu_{ab}^{p} d_{ab}^{2} \tag{1}$$

where p controls the amount of fuzzy overlap between clusters, with smaller values suggesting a less degree of overlap and it is usually greater than 1. In this study, p equals 2. μ_{ab} is the degree of membership of the multi-dimension measured data of the ath pixel in the bth cluster; n and c are the number of pixels and the number of classes in a given image, respectively; and d_{ab} is the distance between the ath measured data and the bth cluster center c_b.

$$\mu_{ab} = \frac{1}{\sum_{m=1}^{c}\left(\frac{d_{ab}}{d_{am}}\right)^{\frac{2}{p-1}}}$$
$$c_b = \frac{\sum_{a=1}^{n}\mu_{ab}^{p} x_a}{\sum_{a=1}^{n}\mu_{ab}^{p}} \tag{2}$$

where x_a is the ath measured data. When the improvement ε in the objective function between two consecutive iterations is not significant, the iteration will stop. In this study, this value was set to 1e-5. To avoid the iterative death loop and to save computational time, the greatest iteration time was predefined as 100.

B. FCM Cloud Detection

There are three types of cloud features used in this study: spectral, statistical, and texture. Owing to the wide ranges of reflectance values shown by the various clouds and land cover objects, the clouds and cloud shadows may be not accurately identified from cloud-free observations using only one given spectral band [13]. Hence, by combining two or more individual bands, some appropriate cloud and cloud shadow features based on spectral information can be acquired to highlight the clouds and cloud shadows while reducing the effects of non-cloud and non-cloud shadow pixels. Additionally, compared with non-cloud regions, cloud regions often have higher intensities and fewer details [32]. Therefore, except when taking the spectral characteristics of clouds into account, statistical features were used in this study. Finally, texture features can reflect the spatial arrangement of spectral information and have been successfully employed for cloud classification and detection [39]–[41]. The opaque clouds are obvious in the images and are easily detected; hence, only spectral and statistical features were used in the initial FCM cloud detection. The most obvious clouds can be extracted through the initial FCM cloud detection, but some thin clouds may be missed because they are not as remarkable as the opaque clouds in the images. Thus, secondary cloud detection may be necessary and more cloud features (the texture features in this study) should be included in the secondary cloud detection process to better extract the missed clouds.

C. Spectral Cloud Features

In general, clouds usually have higher reflectance than the land surface; and thus, in the RGB space, clouds appear white and bright. The HOT index [17] was chosen as the first spectral cloud feature. The HOT index can be calculated as follows:

$$HOT = B_{blue} - 0.5 \times B_{red} \tag{3}$$

where *HOT* represents the HOT values, and B_{blue} and B_{red} indicate the reflectance values of blue and red bands.

Because the clouds are often white and bright in the RGB space, the bright values of pixels were selected as the second spectral cloud feature and they can be calculated as follows:

$$Bright = (B_{blue} + B_{green} + B_{red})/3 \tag{4}$$

where *Bright* is the bright values and B_{green} denotes the reflectance values of the green band.

Additionally, a dark channel was selected as the third spectral cloud feature. The dark channel was originally proposed for haze removal [42] and has been proven to be effective for cloud detection [32]. The dark channel can be acquired as follows:

$$Dark = \min\{B_{blue}, B_{green}, B_{red}\} \tag{5}$$

where *Dark* represents the Dark values. Hence, the spectral cloud features can be regarded as {HOT, Bright, and Dark}.

1) Statistical Cloud Features: Local means and variances were utilized to depict the intensity and details of the original image. For a given band, the local mean and variance can be calculated as follows:

$$M_a = \frac{1}{N}\sum_{r\in\Omega_a}^{N} B_r$$

$$V_a = \sqrt{\frac{1}{N}\sum\nolimits_{r\in\Omega_a}^{N}(B_r - M_a)^2} \tag{6}$$

where M_a and V_a refer to the mean and variance values of the *a*th pixel; B_r is the *r*th pixel of a given band in a local window Ω_a surrounding the *a*th pixel; and *N* is the number of pixels in the local window. The size of the local window was set to 3 and 5 and all the visible bands were considered in this study; thus, 12 statistical features can be acquired in total.

2) Texture Cloud Features: Instead of using the experimental bands directly, we selected the first and second principal components (PC), which account for more than 98% of the original image information in the results of principal component analysis (PCA), to calculate the texture cloud features. The Gabor filter, defined as follows, is thought to be an effective model to identify texture:

$$g(x, y, \lambda, \psi, \sigma, \gamma) = \exp\left(-\frac{x'^2 + \gamma^2 y'^2}{2\sigma^2}\right)\exp\left(i\left(2\pi\frac{x'}{\lambda}\right)\right)$$

$$x' = x\cos\psi + y\sin\psi$$

$$y' = -x\sin\psi + y\cos\psi \tag{7}$$

where λ is the wavelength of the sinusoidal function and, in this study, the wavelength was set to 3 and 4; ψ represents the orientation, and it was set to 0, 45°, 90°, and 135°, respectively; σ is the standard deviation of the Gaussian envelope, which is related to the bandwidth and wavelength; γ is the aspect ratio, which controls the ellipticity of the Gaussian envelope, and it was set to 0.5 in this study. There are 8 texture features generated after the texture features calculation for each PC. Accordingly, 16 texture cloud features can be used further.

4) Feature fusion: After calculating the features, we needed to combine these features into some fundamental feature sets as inputs for the FCM classification. The feature fusion process involves two steps: (1) normalize a variety of features obtained in sections 3.2.1-3.2.3; and (2) select appropriate features and merge these normalized features into the best feature subset. The multi-type features were normalized to [0,1] as follows:

$$f_{nor} = \frac{f - f_{\min}}{f_{\max} - f_{\min}} \tag{8}$$

where f_{nor} denotes normalized feature data; f is raw feature data; and $f_{\max}$ and $f_{\min}$ are the maximum and minimum values of the raw feature data.

In this study, using the multi-type fusion method [43]; we combined the objective features from head to tail. The opaque clouds are obvious in the optical images because of their high reflectance in the visible bands and are relatively easy to identify; therefore, we only used the spectral and statistical cloud features for opaque cloud detection. Meanwhile, some thin clouds may contain various spectral signatures from both clouds and the surface underneath because of their translucency [44]–[46]; thus, it may be difficult to screen them out. Therefore, we added the texture cloud features into the secondary cloud detection. Here, $A = \{a1,a2,a3\}$ are normalized spectral features; $B = \{b1,b2,b3,b4,b5,b6,b7,b8,b9,b10,b11,b12\}$ are normalized statistical features; and $C = \{c1,c2,c3,c4,c5,c6,c7,c8,c9,c10,c11,c12,c13,c14,c15,c16\}$ are normalized texture features. The combined set of *A* and *B* was used for the initial cloud detection and the combined set of *A*, *B*, and *C* was used for the secondary cloud detection.

5) Cloud Detection: After acquiring the combined subsets, we can use the FCM to identify the clouds. As mentioned above, the FCM was used twice in the cloud detection procedure. At each time, the objective pixels were classified into two classes: clouds and non-cloud pixels. The sum of the degrees of memberships of a given pixel in the two clusters was equal to 1. The degree of membership of a given pixel in each cluster was employed as a decision factor to determine which cluster a pixel belonged to. In the initial cloud detection, pixels with larger degrees of memberships in the cloud cluster were deemed as cloud pixels, i.e., the classification threshold was set to 0.5 in the initial detection because of the obvious difference between the cloud and non-cloud pixels. In the secondary cloud detection, the clouds were probably not as easily detected as in the initial detection, so we used (9) to calculate an adaptive threshold in the secondary cloud detection.

$$Thres = mean\{U\} + sd\{U\} \tag{9}$$

where *Thres* is the threshold value, **U** is the set of degrees of membership of the non-cloud pixels after the initial cloud detection in the cloud cluster, and *mean{.}* and *sd{.}* are the mean and standard deviation values. If the degrees of membership of non-cloud pixels after the initial cloud detection in the cloud cluster were greater than the threshold value, they were deemed potential cloud pixels.

A cloud verification step based on the cluster centers was operated to determine whether the potential cloud pixels were real ones. If the dissimilarity between the cloud cluster and the non-cloud cluster is relatively large, we can deduce that the

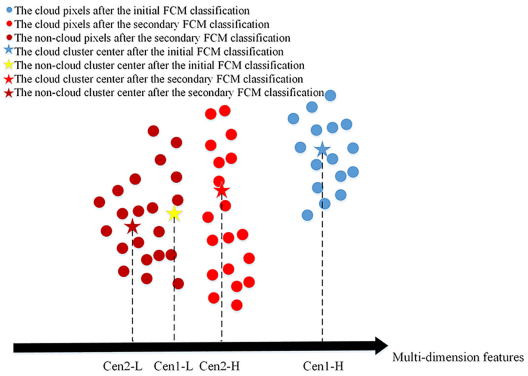

Fig. 2. Locations of four cluster centers on the axis of multi-dimension features.

cloud and non-cloud pixels are reasonably separated; otherwise the cloud and non-cloud pixels may be mistakenly classified. In this study, the cloud and non-cloud cluster centers in the initial cloud detection were denoted Cen1-H and Cen1-L, and the cloud and non-cloud cluster centers in the secondary cloud detection were denoted Cen2-H and Cen2-L. The lengths of the cluster centers are equal to the number of features used in each FCM classification. Because the cloud feature subsets used in the initial and secondary cloud detection were different, the cluster centers with the overlapped features were used for distance calculation. The locations of these four centers on the axis of multi-dimension features are shown roughly in Fig. 2. If the distance between Cen2-H and Cen2-L is large enough, then we can deduce that the secondary cloud detection is necessary and the cloud pixels obtained from the initial and secondary cloud detection are both deemed as clouds; otherwise, we can deduce that the cloud and non-cloud pixels from the secondary cloud detection cannot be effectively classified and only the cloud pixels obtained from the initial cloud detection are deemed as clouds. We used the normalized distance to indicate the distance between Cen2-H and Cen2-L as follows:

$$Dis = \frac{Cen2{-}H - Cen2{-}L}{Cen1{-}H - Cen2{-}L} \tag{10}$$

where *Dis* is the normalized distance between the cloud and non-cloud cluster centers in the secondary cloud detection. If the normalized distance is larger than a threshold, the secondary cloud detection can be considered to be necessary. In this study, the threshold was set to 0.25.

C. FCM CCloud Shadow Detection

1) Spectral Cloud Shadow Feature: In cloud shadow detection, given that the solar radiation is blocked by clouds, the cloud shadows are mainly illuminated by scattered light. Hence, the shadowed pixels of the NIR band are much darker than their surroundings because of the weaker atmospheric scattering at longer wavelengths [2]. However, water bodies are also easily considered as cloud shadows in NIR band because they can absorb more radiation at longer wavelengths [6]. Hence, the water pixels were excluded from the cloud shadow detection in this study. As water is generally dark whereas land is relatively bright in the NIR band, the NIR band reflectance is suitable for identifying water. Moreover, the normalized difference vegetation index (NDVI) and the normalized difference water index (NDWI) are also good indices for differentiating water pixels from land pixels [33], [47]. In general, the NDVI values of water pixels are less than 0.1 and the reflectance of the NIR band of water pixels is usually less than 0.05. However, the influence of thin clouds and turbid conditions may cause the water pixels to have large reflectance values [2]; therefore, another water test based on NDVI values and the reflectance of the NIR band is also used. Additionally, due to the influence of the reflectance of thick cloud shadow in the NIR band [33], the threshold for NDWI was set to 0.1.

$$\begin{aligned} water_pixels = {} & NDWI > 0.1 \\ & ((NDVI < 0.01\ B_{NIR} < 0.11)|(NDVI \\ & < 0.1\ B_{NIR} < 0.05)) \end{aligned} \tag{11}$$

where *water_pixels* refers to the pixels indicating water and B_{NIR} is the reflectance values of the NIR band. *NDVI* and *NDWI* are calculated as follows:

$$\begin{aligned} NDVI &= \frac{B_{NIR} - B_{red}}{B_{NIR} + B_{red}} \\ NDWI &= \frac{B_{green} - B_{NIR}}{B_{green} + B_{NIR}} \end{aligned} \tag{12}$$

As cloud shadows are usually darker than their surroundings, they are mostly located at places with regional minima. Hence, a "flood-fill" morphological transformation [48] was employed to extract potential local cloud shadow areas. For grayscale images, this transformation can increase the intensity values of dark areas surrounded by lighter areas to the same intensity level as the surrounding pixels. Then the dissimilarity between the original image and the filled image after the transformation can be used to determine the potential cloud shadows. The cloud shadow index for non-water pixels can be acquired using the following calculation:

$$SI = Flood{-}fill(\mathrm{B}_{NIR}){-}\mathrm{B}_{NIR} \tag{13}$$

where *SI* represents the cloud shadow index and *Flood-fill* indicates the "flood-fill" morphological transformation. Even though the "flood-fill" morphological transformation has been used in cloud shadow detection [2], [6], there is still a limitation when using this transformation to detect cloud shadows. An example of cloud shadow detection is shown in Fig. 3. The area marked by the yellow square is a small clear-sky region surrounded by clouds, which is treated as a "hole" in the morphological transformation; thus, this whole clear-sky region will be labeled as either cloud shadow or non-cloud shadow. However, only some parts of this region are virtually cloud shadows. Hence, using the "flood-fill" morphological transformation directly may mislabel the clear-sky pixels. Here, we modified the cloud shadow index calculation. First, we used the "flood-fill" morphological transformation to fill the "holes" in the image; and then we extracted the filled and non-filled areas; next, the cloud shadow index was individually calculated

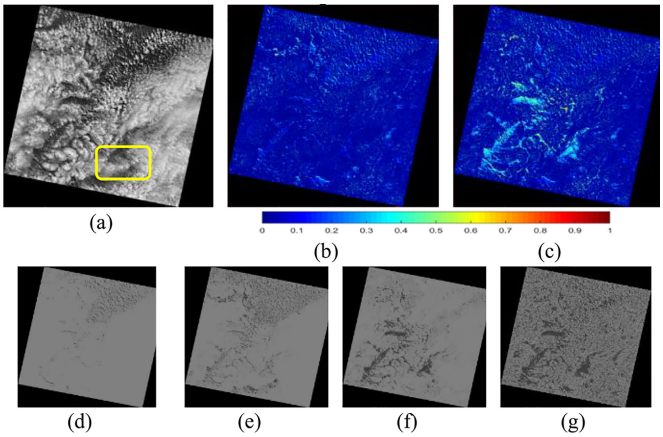

Fig. 3. Example of initial cloud shadow detection. (a) Original Landsat OLI scene (p102_r80 and 20140410). (b)-(c) Normalized cloud shadow indices by using the modified scheme (MS) and using the "flood-fill" transformation directly (OS). (d) Reference image of the cloud shadows. (e)-(f) Initial cloud shadow pixels acquired by applying the FCM to the normalized cloud shadow indices obtained from MS and OS. (g) Initial cloud shadow pixels by using Fmask method.

for the filled areas and non-filled areas; then, the cloud shadow index was normalized by using (8); finally, the FCM was applied to the cloud shadow index to acquire the initial cloud shadow pixels. We set a higher priority for cloud in this study. Fig. 3(b) and 3(c) show the normalized cloud shadow index using the modified scheme (MS) and the "flood-fill" transformation directly (original scheme (OS)). For the areas surrounded by clouds, such as the marked area, the cloud shadow index values obtained from OS are relatively larger than those obtained from MS, so these areas are more likely to be classified as cloud shadows as a whole. Fig. 3(d) depicts the reference image of cloud shadows; Fig. 3(e) and 3(f) present the initial cloud shadow pixels acquired by applying the FCM to the normalized cloud shadow indices obtained from MS and OS; Fig. 3(g) shows the initial cloud shadow pixels by using the Fmask method. As shown in Fig. 3(f), the relatively large cloud shadow index values at the "hole" regions means that these are mislabeled as cloud shadows while the real cloud shadow pixels in the upper part of the image are missing. The initial cloud shadow pixels obtained from the Fmask method can detect the cloud shadow pixels in the upper part of image, but the "hole" regions are also classified as cloud shadows. Even though some clear-sky pixels at the "hole" regions are mislabeled as cloud shadows, compared to the other two results, the initial cloud shadow pixels obtained from MS are closer to the reference image of cloud shadows. In the FCM cloud shadow detection, the pixels with larger degrees of memberships in the cloud shadow cluster were deemed as cloud shadow pixels.

2) Cloud and Cloud Shadow Matching: The initial cloud shadow pixels may contain some mislabeled pixels, such as dark objects and topographic cloud shadows. The cloud shadows cannot exist without clouds [2]–[3]; thus, the spatial geometric relationship between the clouds and cloud shadows can reduce commission errors of cloud shadow detection. For most whisk-broom sensors, the projection of cloud shadows on the surface

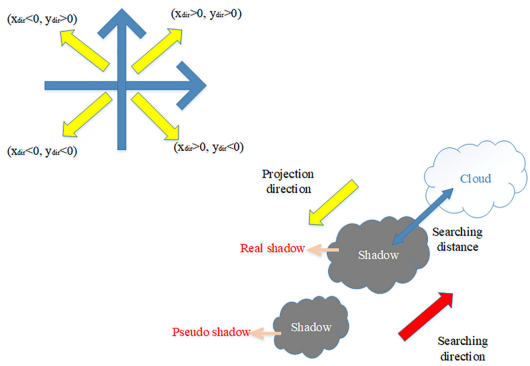

Fig. 4. The process of cloud and cloud shadow matching.

can be acquired as follows [49]:

$$x_{s_img} = x_{c_img} + h_c(\tan\theta_{viewing}\sin\phi_{viewing} - \tan\theta_{solar}\sin\phi_{solar})$$
$$y_{s_img} = y_{c_img} + h_c(\tan\theta_{viewing}\cos\phi_{viewing} - \tan\theta_{solar}\cos\phi_{solar}) \quad (14)$$

where $x_{\mathrm{c_img}}$ and$y_{\mathrm{c_img}}$ indicate the coordinates of a given cloud pixel; $x_{\mathrm{s_img}}$ and $y_{\mathrm{c_img}}$ represent the coordinates of its corresponding cloud shadow pixel; h_c is height of the cloud above the surface; $\theta_{viewing}$ and θ_{solar} are the viewing and solar zenith angles, respectively; and $\Phi_{viewing}$ and Φ_{solar} are the viewing and solar azimuth angles (clockwise from the true North), respectively. The values of $\theta_{viewing}$, θ_{solar}, $\Phi_{viewing}$, and Φ_{solar} can be found in the metadata files, although h_c is an unknown parameter usually set with the help of the thermal band [2]. Even though the heights of clouds are difficult to estimate, the directions of the cloud shadows can be obtained accurately as follows:

$$x_{dir} = \tan\theta_{viewing}\sin\phi_{viewing} - \tan\theta_{solar}\sin\phi_{solar}$$
$$y_{dir} = \tan\theta_{viewing}\cos\phi_{viewing} - \tan\theta_{solar}\cos\phi_{solar} \quad (15)$$

where x_{dir} and y_{dir} are the projection direction of cloud shadows that do not change at different places in one image. As shown in Fig. 4, in this study, we defined four reprojection directions including 45°, 135°, 225°, and 315° based on the values of x_{dir}, y_{dir}. For the cloud shadow pixels, a searching window along the searching direction, which is opposite to the corresponding reprojection direction, was constructed. If cloud pixels exist in the searching window, then the cloud shadows can be deemed as real ones; otherwise, they are considered as pseudo cloud shadows and removed. The window size can be determined visually, and we will discuss the influence of the searching window size on the cloud shadow detection in Section 5.3. After cloud and cloud shadow matching, the holes in the cloud shadow mask were filled to obtain the final cloud shadow mask.

D. Accuracy Assessment

Four metrics including producer agreement rate (*PAR*), user agreement rate (*UAR*), non-agreement rate (*NAR*), and the ratio

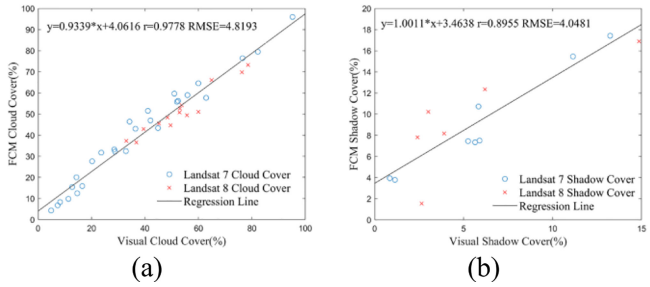

Fig. 5. (a) Comparison of cloud cover between FCM and references. (b) Comparison of cloud shadow cover between FCM and references.

of PAR to NAR (*RER*) were used to quantitatively assess the effectiveness of the FCM. They are defined as:

$$Pro{-}Agreement = \frac{NCS}{NCST} \tag{16}$$

$$User{-}Agreement = \frac{NCS}{NCSR} \tag{17}$$

$$Non{-}Agreement = \frac{CSN + NCS}{NT} \tag{18}$$

$$RER = \frac{Pro{-}Agreement}{Non{-}Agreement} \tag{19}$$

where *NCS* is the number of correct cloud (cloud shadow) pixels, *NCST* is the number of cloud (cloud shadow) pixels in ground truth, *NCSR* is the number of cloud (cloud shadow) pixels in the detected results, *CSN* indicates the number of clouds (cloud shadow) pixels classified as non-cloud (non-cloud shadow) pixels, *NCS* indicates the number of non-clouds (non-cloud shadow) pixels classified as cloud (cloud shadow) pixels, and *NT* is the number of pixels of the original image.

Because some methods may obtain a high *PAR* but also bring many errors, while some methods can have low *NAR* but also low *PAR*, one combined metric (*RER*) based on *PAR* and *NAR* is used to measure the performance [30]. The higher it is, the better.

IV. Results

A. FCM Results

As shown in Fig. 5(a), the estimates of percent cloud cover obtained from the FCM and manual interpretation are similar, with a correlation coefficient of more than 0.97. The slope of the regression line is 0.9339, with an interception of 4.06% and a relatively small root mean square error (RMSE) of 4.8193. Meanwhile, the difference of the estimates of percent cloud shadow cover between the FCM and manual interpretation is not obvious (Fig. 5b), with a correlation coefficient of 0.8955. The slope of the regression line is 1.0011, with an interception of 3.4638% and a small RMSE of 4.0481. Hence, the percentages of cloud and cloud shadow cover can reflect that the FCM is effective on cloud and cloud shadow detection.

Except for the statistical analysis, we also took two Landsat 7 ETM+ and one Landsat 8 OLI images as examples to show the performance of the FCM.

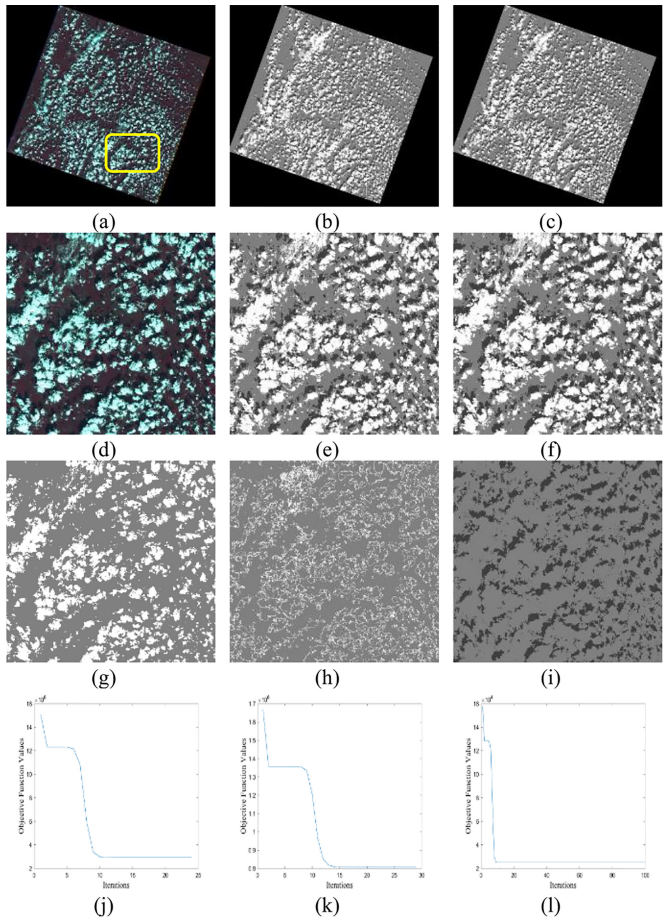

Fig. 6. Landsat image scene and cloud and cloud shadow detection results of applying the fuzzy c-means (FCM) algorithm. (a) NIR-red-green composite image of Landsat 7 (Scene ID: p138r16_20010613). (b) Reference map. (c) Cloud and cloud shadow detection results obtained using the FCM algorithm. (d)–(f) Corresponding local zoomed maps labeled using the yellow square in (a). (g)-(h) Clouds after the initial and secondary detections. (i) Cloud shadow mask. (j)-(l) Objective function values of the initial and secondary cloud and cloud shadow detections.

The NIR-red-green composite image of the Landsat 7 ETM+ image (Scene ID: p138r16) on June 13, 2001, the reference map, and the result obtained by using the FCM are given in Fig. 6(a)-(c) and the local zoomed area marked by a yellow square in Fig. 6(a) is also used to highlight the performance of the FCM [Fig. 6(d)-(f)]. Both thick and thin clouds can be found in the image and the small patches of clouds are evenly distributed. The cloud masks obtained from the initial and secondary cloud detection are shown in Fig. 6(g)-(h) and the cloud shadow mask is shown in Fig. 6(i). The searching window size for cloud shadow detection was set to 70 pixels through visual determination. As shown in Fig. 6, from the whole scene maps, the clouds and cloud shadows are precisely identified, and the detected output is similar to the reference map. Especially, the thin clouds around the opaque clouds, which are difficult to detect, are also well extracted. From the local zoomed maps, it can be observed that the identified clouds and their accompanying cloud shadows are both consistent with the reference image. The shapes and spatial locations of thick and

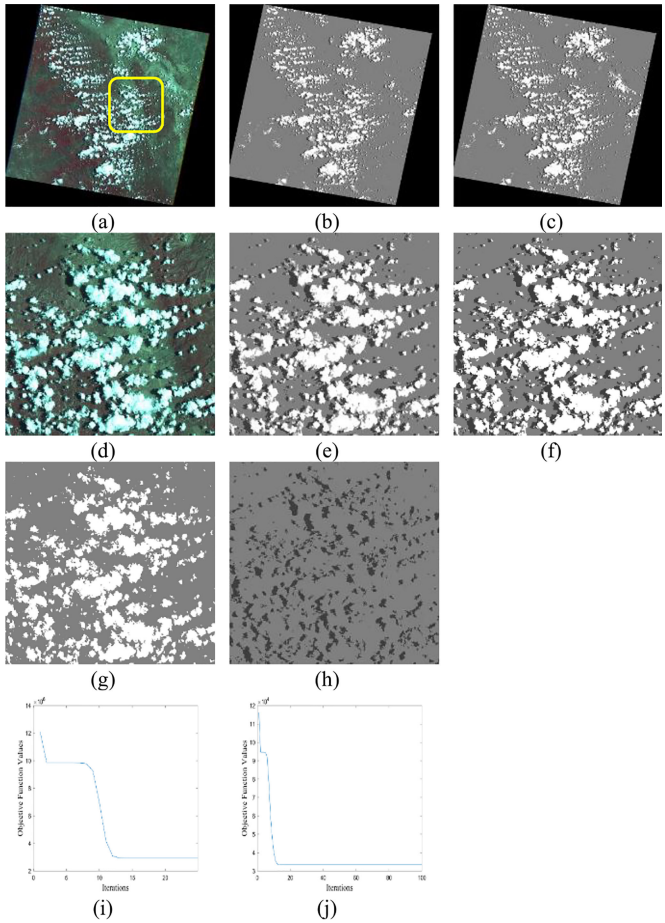

Fig. 7. Landsat image scene and cloud and cloud shadow detection results of the FCM. (a) NIR-red-green composite image of Landsat 7 (Scene ID: p31r43_20010615). (b) Reference map. (c) Cloud and cloud shadow detection results by using the FCM. (d)-(f) Corresponding local zoomed maps labeled using the yellow square in (a). (g) Cloud mask. (h) Cloud shadow mask. (i)-(j) Objective function values of the cloud and cloud shadow detections.

thin clouds are well described, which suggests the effectiveness of the FCM. Additionally, it can be noted that the obvious and thick clouds can be accurately detected by using the initial cloud detection, whereas the thin clouds around the thick clouds can be further detected in the secondary cloud detection. Finally, as shown in Fig. 6(j)-(l), the objective function values in cloud and cloud shadow detection using the FCM converge quickly, and thus, the proposed method can be used for large-scale images.

Another Landsat 7 ETM+ image (p31r43) on June 15, 2001 was also used to evaluate the performance of the FCM. The clouds are distributed along the northwest-southeast direction and the patches of clouds are relatively small. In this experiment, the secondary cloud detection was excluded because the distance between the cluster centers obtained in the secondary cloud detection was not greater than the predefined threshold. Therefore, only the cloud pixels from the initial cloud detection were deemed as clouds. The NIR-red-green composite ETM+ image, the reference map, and the output of the FCM are shown in Fig. 7(a)-(c). A local zoomed area marked by the yellow square in Fig. 7(a) was used to demonstrate the detection performance (Fig. 7(d)-(f)). The cloud and cloud shadow pixels are individually shown in Fig. 7(g)-(h). In this experiment, the searching window size for cloud shadow detection was set to 50 pixels. The FCM performs well by precisely identifying the clouds and cloud shadows and reducing the confusions caused by bright surface objects, even though some land pixels in the right-upper image are mislabeled as clouds. Moreover, we can see that although only the cloud pixels from the initial cloud detection were deemed as clouds, the output of the FCM can still capture the main clouds. The local zoomed maps show that the shapes and locations of clouds and cloud shadows are well preserved and the bright background in the middle of the zoomed image does not affect the performance of the FCM. Similarly, the objective function values in cloud and cloud shadow detection converge rapidly after several iterations.

A Landsat 8 OLI image (p16r50) from February 10, 2014 was used to assess the performance of the FCM. The clouds are evenly distributed and in relatively small patches in the image. The NIR-red-green composite OLI image, the reference map, and the output of the FCM are shown in Fig. 8(a)-(c). A local zoomed area marked by the yellow square in Fig. 8(a) was used to demonstrate the detection performance (Fig. 8(d)-(f)). The cloud and cloud shadow pixels are shown individually in Fig. 8(g)-(i). In this experiment, the size of the searching window for cloud shadow detection was set to 55 pixels. As shown in Fig. 8, most clouds and their accompanying cloud shadows were precisely detected, with edges and details of both pretty preserved. As in the first experiment, the initial cloud detection can capture the main obvious clouds, and the thin clouds around the thick clouds can be identified in the secondary cloud detection. Additionally, with the help of the modified cloud shadow index calculation, "hole" areas—such as the area marked by the dark blue circle in Fig. 8(b)—were not deemed as cloud shadows as a whole. However, many pseudo cloud shadows were not removed because of the influence of dark land objects and the existence of clouds in neighboring areas, which may decrease the accuracy of cloud shadow detection. Additionally, the objective function values [Fig. 8(j)-(l)] in cloud and cloud shadow detection also converge rapidly after several iterations.

B. Comparisons With Other Methods

In this section, the FCM results are compared with the results obtained from two state-of-the-art methods: Fmask and SVM. The Fmask method [2] has been used by the USGS to generate the standard cloud mask for Landsat images, and the SVM method can be regarded as a hard clustering technique and has been widely used. The Fmaks method was implemented using the Calculate Cloud Mask Using Fmask Algorithm module in ENVI 5.3 and all spectral, statistical and texture features were used in SVM method for training. Similar with [32], Ostu method was first used to determine the cloud/non-cloud pixels, and then 5000 cloud pixels and 5000 non-cloud pixels were selected for model tuning. The results of these two methods are typical and representative. Fig. 9 shows the reference maps used

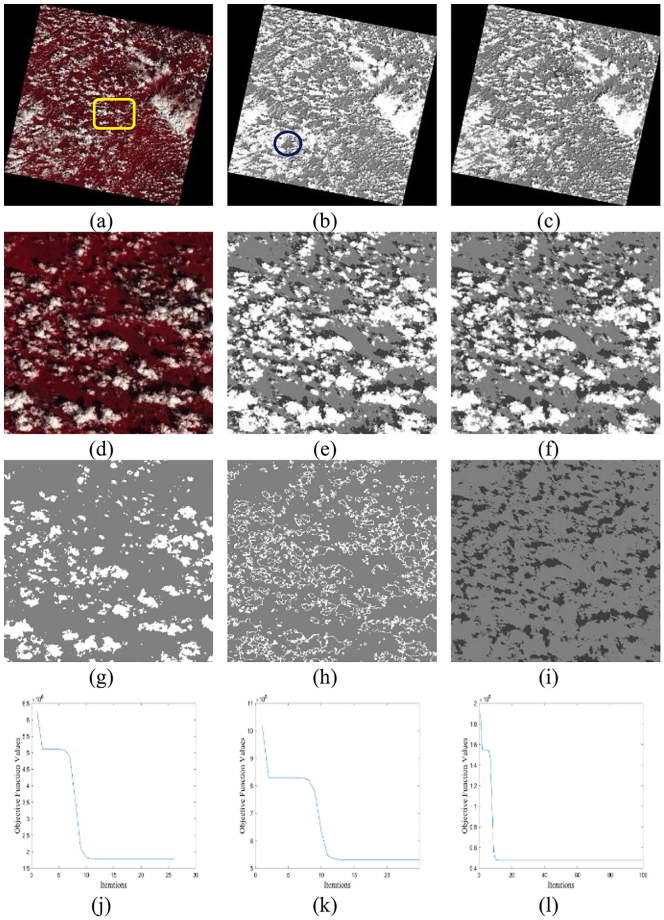

Fig. 8. Landsat image scene and cloud and cloud shadow detection results of the FCM. (a) NIR-red-green composite image of Landsat 8 (Scene ID: p16r50_20140210). (b) Reference map. (c) Cloud and cloud shadow detection results by using the FCM. (d)-(f) Corresponding local zoomed maps labeled using the yellow square in (a). (g)-(h) Cloud masks after the initial and secondary cloud detections. (i) Cloud shadow mask. (j)-(l) Objective function values of the initial and secondary cloud and cloud shadow detections.

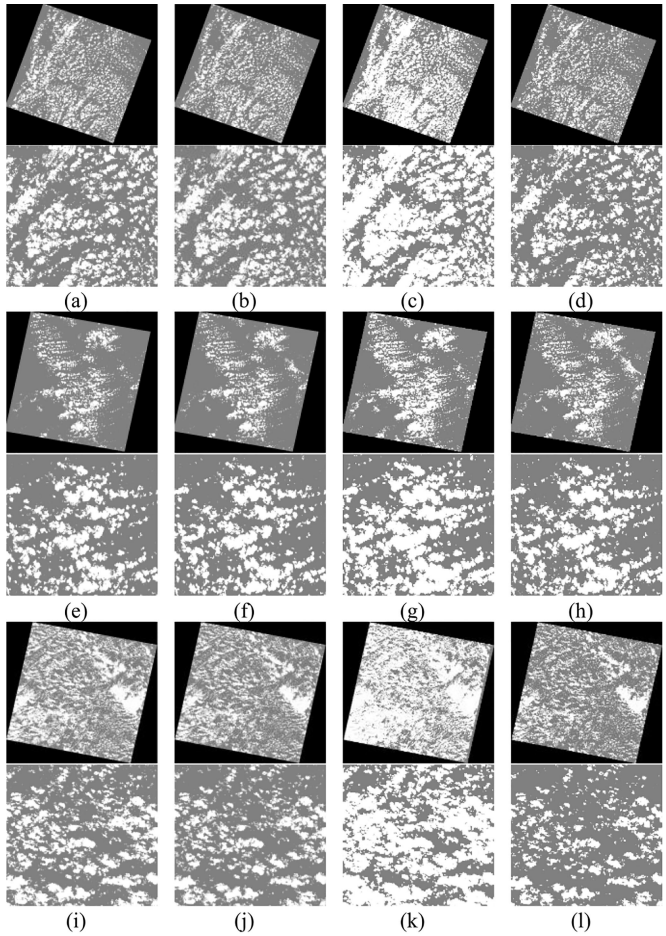

Fig. 9. Results of three Landsat scenes (p138r16, p31r43, p16r50). (a), (e), (i) Reference maps. (b)-(d), (f)-(h), (j)-(l) Results of cloud detection by using the FCM, Fmask, and SVM methods. The lower images in each row are the corresponding local zoomed maps marked in Fig. 6(a), 7(a), and 8(a).

in Section 4.1 and the results obtained from the FCM, Fmask, and SVM methods. The local zoomed images marked in Fig. 6(a), 7(a), and 8(a) are also used to show the differences among these three results. In general, the results obtained from the FCM are closer to the reference maps for these three images with regard to spatial details, suggesting that the proposed method has stronger stability and better performance than the other two methods. Obviously, the results of the Fmask method seem to be overestimated: although the main clouds can be captured, many clear-sky pixels are mislabeled as clouds pixels, and thus, the *PAR*s and *NAR*s are both relatively high. The results obtained from the SVM method are similar to those from the FCM. However, as the classification process is operated only once, some thin clouds and details are missed.

As shown in Table II, for all Landsat 7 ETM+ and Landsat 8 OLI scenes, although the average *PAR* obtained from the FCM is a little lower than that from the Fmask method, but the average *NAR* of the Fmask method is relatively higher; in addition, the average *PAR* and *NAR* of the FCM are both superior to the SVM method. Hence, the FCM has the highest average *RER* among

TABLE II
STATISTICAL COMPARISONS OF THESE THREE METHODS

Sensor		Average PAR	Average NAR	Average UAR	Average RER
Landsat 7	FCM	0.9367	0.0611	0.8745	24.0387
	Fmask	0.9819	0.1108	0.6490	13.6749
	SVM	0.8794	0.0842	0.8915	22.2956
Landsat 8	FCM	0.9363	0.0517	0.9616	21.3313
	Fmask	0.9762	0.1481	0.7104	7.1552
	SVM	0.7902	0.1064	0.9960	8.6884

these three methods, followed by SVM method. The Fmask method has the highest average *PAR* and *NAR*, suggesting that Fmask can capture most of the clouds but also misclassify many clear-sky pixels as clouds. Compared to the FCM method, the SVM method has lower average *PAR* but higher average *UAR*, which means some real cloud pixels may be undetected by the SVM method. Similarly, the lowest average *UAR* obtained from the Fmask method indicates the results may contain some pseudo cloud pixels.

The *PAR* and *NAR* of each scene are similar [Fig. 10(a) and (c)]. The *PAR*s of the FCM are slightly lower than those of Fmask

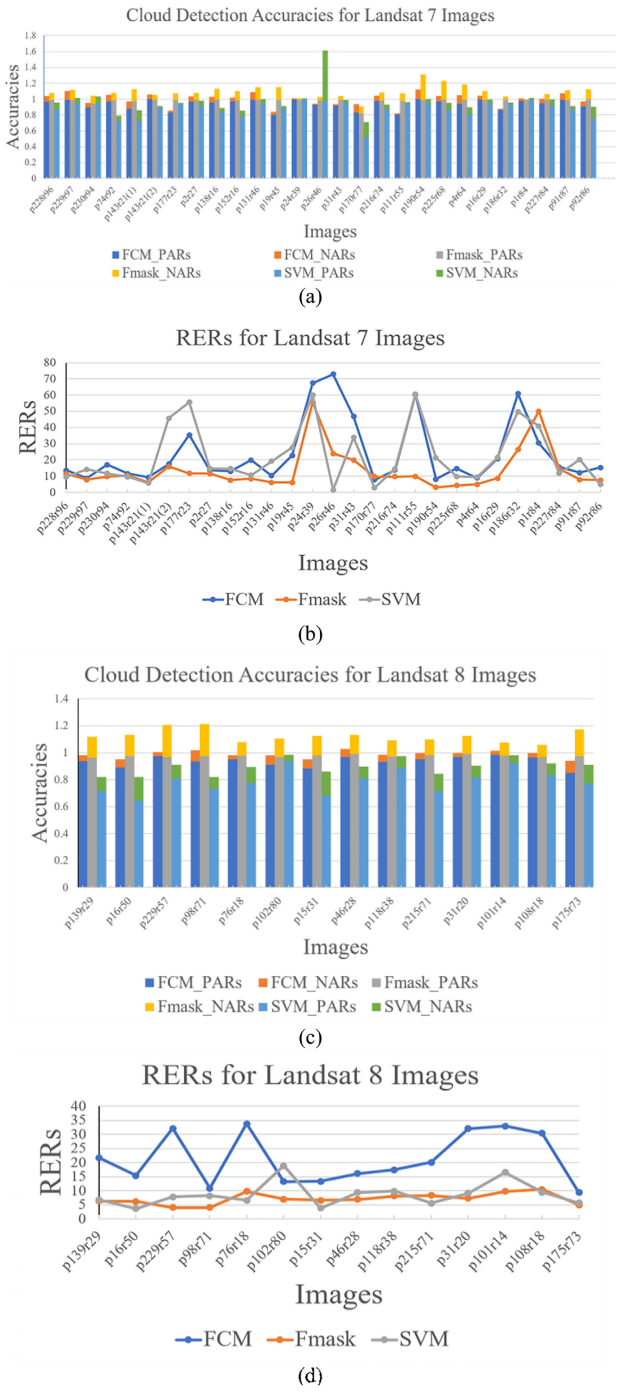

Fig. 10. (a), (c) *PAR*s and *NAR*s obtained from the three methods for Landsat ETM+ scenes and OLI scenes. (b), (d) *RER*s obtained from the three methods for Landsat ETM+ scenes and OLI scenes.

method, but they are higher than those of the SVM method. Moreover, the *NAR*s of the FCM are relatively lower than those of the other two methods. In addition, the *RER*s of the FCM are the highest among these three methods for most scenes, especially for Landsat 8 OLI scenes. All the statistical results show that the FCM can acquire a better balance between the cloud pixel detection and non-cloud pixel exclusion.

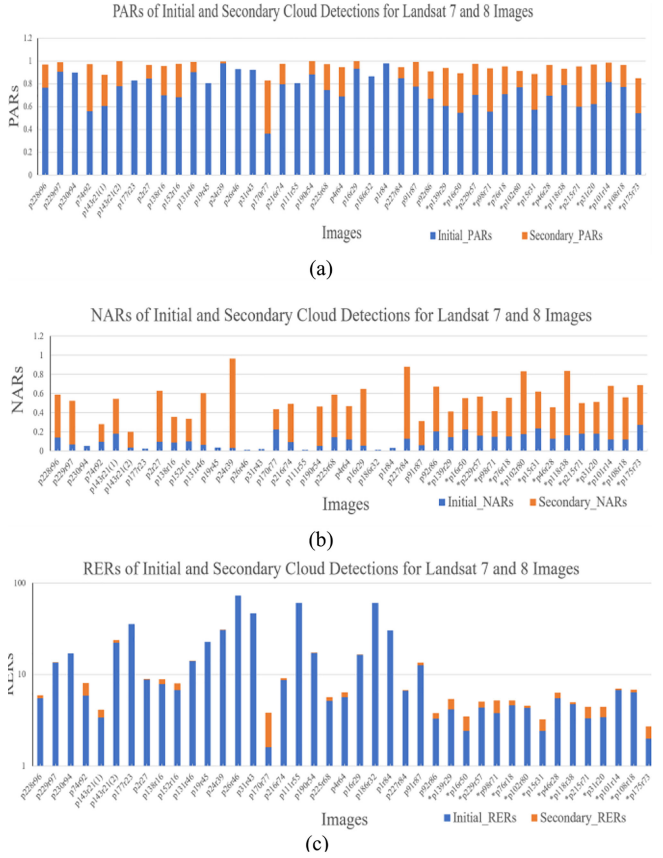

Fig. 11. (a-b) *PAR*s and *NAR*s of initial and secondary cloud detections. (c) *RER*s of initial and secondary cloud detections. *indicates Landsat 8 OLI scences.

V. Discussion

A. Contributions of the Initial and Secondary Cloud Detections

Because there are two cloud detection processes in the FCM, the contributions to cloud detection of these two processes are discussed. The secondary cloud detection was not applied to eight Landsat 7 ETM+ scenes, so these images were not discussed in this section. As shown in Fig. 11, for most scenes, the initial cloud detection can obtain relatively higher *PAR*s and *RER*s and lower *NAR*s than the secondary cloud detection, suggesting that the initial cloud detection has better detection accuracy. This is because the obvious clouds are mostly detected in the initial cloud detection, whereas the secondary cloud detection aims at screening the thin clouds around the thick clouds which are more difficult to detect. Additionally, the secondary cloud detection seems to be more significant for the scenes with massive thin clouds, such as the Landsat 7 ETM+ scene (p170r77). Meanwhile, even though the secondary cloud detection can mislabel some clear-sky pixels as clouds, it can also enhance the *PAR*s. When the secondary cloud detection is considered, the average *PAR* increases from 0.7190 to 0.9506, and the average *RER* increases from 7.6931 to 18.2154. Hence, the secondary cloud detection seems to be necessary if the

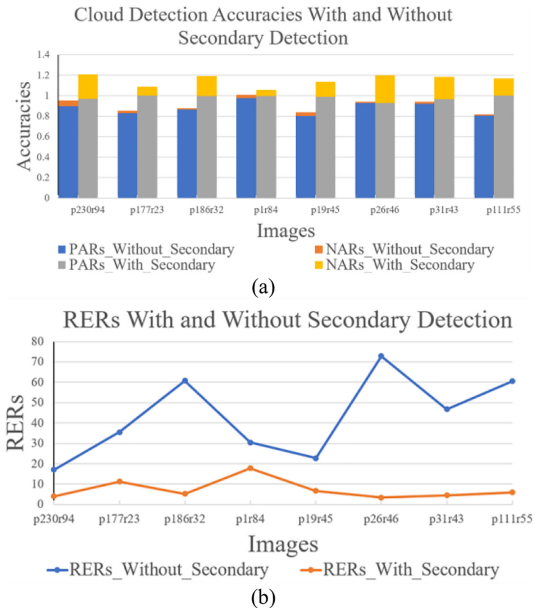

Fig. 12. (a) *PAR*s and *NAR*s with and without the secondary cloud detections. (b) *RER*s with and without the secondary cloud detections.

distance between the cluster centers in the secondary cloud detection is greater than the predefined threshold.

B. Necessity of the Secondary Cloud Detection

The secondary cloud detection was not applied to eight Landsat 7 ETM+ images because of the relatively small distance between the cluster centers obtained in the secondary cloud detection. In this section, the secondary cloud detection was also applied to these eight images to analyze whether the exclusion of the secondary cloud detection is correct. The *PAR*s and *NAR*s with and without the secondary cloud detection are presented in Fig. 12a and their corresponding *RER*s are depicted in Fig. 12b. It can be easily observed that the secondary cloud detection can enhance *PAR*s and *NAR*s, simultaneously. When considering the secondary cloud detection, the average *PAR* can increase from 0.8788 to 0.9811, and meanwhile, the average *NAR* also increases from 0.0254 to 0.1731. Additionally, the *RER*s without the secondary cloud detection are much higher than those with the secondary cloud detection, and the average *RER* decreases from 43.3221 to 7.3263 when the secondary cloud detection was operated. Hence, it is reasonable that the secondary cloud detection was not applied to these scenes. Besides, it can be noted that, except for these eight images, the secondary cloud detection can enhance the average *RER* from 7.6931 to 18.2154, suggesting that the exclusion of the secondary cloud detection for these eight images is necessary and the threshold for determining the necessity of the secondary cloud detection is reasonably set.

A Landsat 7 scene (Scene ID: p230r94_20011226) was used as an example to demonstrate the necessity of the secondary cloud detection. In this study, the secondary cloud detection was not operated on this image because the normalized distance

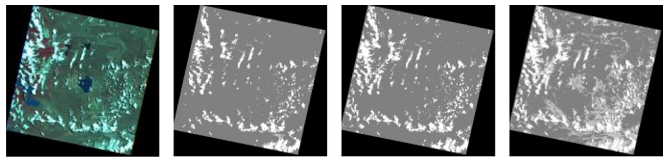

Fig. 13. Results with and without the secondary cloud detection. (a) NIR-red-green composite image of Landsat 7 (Scene ID: p230r94_20011226). (b) Reference map. (c) Result of FCM method without the secondary cloud detection. (d) Result of FCM method with the secondary cloud detection.

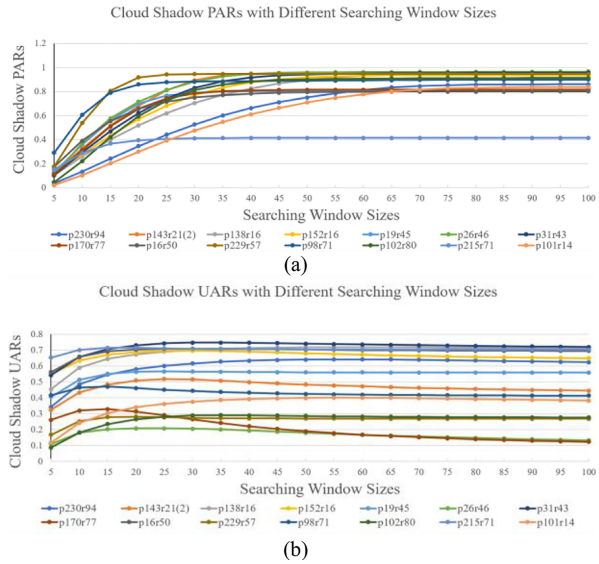

Fig. 14. (a) *PAR*s of cloud shadows with different searching window sizes. (b) *UAR*s of cloud shadows with different searching window sizes.

between the cloud and non-cloud cluster centers in the secondary cloud detection was smaller than the predefined threshold. In this section, we regarded the cloud pixels generated in the secondary cloud detection as clouds. As shown in Fig. 13, most real clouds can be extracted in the initial cloud detection, while some pseudo clouds can be found during the secondary cloud detection. Hence, the exclusion of the secondary cloud detection for this scene is reasonable.

C. Searching Window Size for Cloud Shadow Detection

The influence of the searching window size on the cloud shadow detection are discussed based on a number of experiments. In total, 14 reference maps including 8 Landsat ETM+ and 6 Landsat OLI scenes contain manual cloud shadow masks, so they were selected in this section. Both *PAR* and *UAR* were utilized to discuss the influence of the searching window size. The change trend curves of *PAR*s and *UAR*s with various searching window sizes for the 14 scenes are shown in Fig. 14. As shown in Fig. 14, it can be observed that with the increase in the searching window size, *PAR*s increase steeply at the beginning, and then they stabilize when the searching window sizes reach some specific values. As for *UAR*s, they slightly increase at the

beginning, and then they change little with the increment in the searching window sizes. Additionally, *UAR*s may slightly decrease for some images with the increase in the searching window sizes, which is probably caused by the misclassification in the initial cloud shadow detection using the FCM. Some dark land materials, such as water bodies, may be mislabeled as cloud shadow pixels and larger searching window sizes may contain more mislabeled cloud shadow pixels, thus causing *UAR*s to decrease. Actually, when the searching window sizes reach some specific values, *PAR*s and *UAR*s are both stable and less sensitive, and hence, the searching window sizes can be visually determined and easily fine-tuned. Additionally, it is better not to set the searching window size too large or too small. If the searching window size is too small, some real cloud shadow pixels may be excluded; and if the searching window size is too large, many pseudo cloud shadow pixels may be included, thus lowering the *UAR*s.

VI. Conclusion

In this work, we proposed a cloud and cloud shadow detection method based on the fuzzy c-means algorithm for multi-spectral satellite sensors with visible and NIR bands. Instead of classifying the objective pixels into one specific class, in fuzzy clustering, the data points can belong to more than one cluster, and are each associated with certain membership grades that represent the degree to which they belong to the different clusters. Hence, fuzzy clustering can better characterize the status of one given pixel belonging to clouds or non-clouds. By operating the FCM twice, not only can the thick and obvious clouds be detected, but the thin clouds around the thick clouds can also be better extracted. Additionally, a modified cloud shadow index calculation was proposed to characterize the cloud shadow features better. Taking the reprojection direction and the spatial geometric relationship between clouds and their accompanying cloud shadows into account, a rapid cloud and cloud shadow matching strategy was used to exclude some pseudo cloud shadows. In total, 41 scenes including 27 Landsat ETM+ images in eight latitude zones and 14 Landsat OLI images comprising seven land cover types, including barren, forest, grass, shrubland, urban, water, and wetlands areas, with percentages of cloud cover ranging 4.99% to 97.63%, were utilized to validate the effectiveness of the FCM. The thick and thin clouds along with their associated cloud shadows can be precisely detected by using the FCM. Compared with the Fmask method, the FCM has relatively lower *PAR*s, but fewer clear-sky pixels were misclassified as clouds; compared with the SVM method, the FCM has higher *PAR*s and lower *NAR*s, which means that the FCM can achieve better cloud detection accuracy. The results demonstrate that the FCM can acquire a better balance between cloud pixel detection and non-cloud pixel exclusion. Additionally, the FCM is designed for sensors with both visible and NIR bands, and therefore, it can also be applied for other satellite images with similar spectral channels. Therefore, the lower requirement of input bands can enhance the applicability of the proposed method. In addition, fewer predefined parameters in the FCM is also a typical characteristic.

However, there is still space for the enhancement of the FCM. First, if the satellite image is totally clear-sky or is completely occupied by clouds, the classification process may fail. In addition, the threshold for determining the necessity of the secondary cloud detection and the searching window size for cloud shadow detection are both set subjectively, and thus, some errors may be included. Third, the FCM does not currently have a snow detection module, which means that the snow in the image may be mislabeled as clouds. Actually, most cloud detection methods with a snow detection module may be similarly affected by snow [13]. Fourth, some bright land objects may be identified as clouds, as in the FCM results shown in Fig. 7(c). Hence, more appropriate cloud features, such as features obtained from the IHOT algorithm, should be incorporated in the FCM to reduce the influence of very bright pixels. All of these issues will be addressed in future work.

Acknowledgment

The authors would like to thank the Institute of Geographic Sciences and Natural Resources Research, University of the Chinese Academy of Sciences, the National Marine Data and Information Service, and Tianjin University for their support. The authors would also like to thank the anonymous reviewers who provided valuable comments, which greatly enhanced the quality of the manuscript.

References

[1] R. R. Irish, J. L. Barker, S. N. Goward, and T. Arvidson, "Characterization of Landsat-7 ETM+ automated cloud-cover assessment (ACCA) algorithm," *Photogrammetric Eng. Remote Sens.*, vol. 72, no. 10, pp. 1179–1188, 2006.

[2] Z. Zhu and C. E. Woodcock, "Object-based cloud and cloud cloud shadows detection in Landsat imagery," *Remote Sens. Environ.*, vol. 118, pp. 83–94, 2012.

[3] Z. Zhu, S. X. Wang, and C. E. Woodcock, "Improvement and expansion of the Fmask algorithm: Cloud, cloud cloud shadows, and snow detection for Landsat 4-7, 8, and Sentinel-2 images," *Remote Sens. Environ.*, vol. 159, pp. 269–277, 2015.

[4] T. Wu, X. Y. Hu, Y. Zhang, L. L. Zhang, P. J. Tao, and L. P. Lu, "Automatic cloud detection for high resolution satellite stereo images and its application in terrain extraction," *ISPRS J. Photogrammetry Remote Sens.*, vol. 121, pp. 143–156, 2016.

[5] Y. C. Zhang, W. B. Rossow, A. A. Lacis, V. Oinas, and M. I. Mishchenko, "Calculation of radiative fluxes from the surface to top of atmosphere based on ISCCP and other global data sets: Refinements of the radiative transfer model and the input data," *J. Geophys. Res. Atmos.*, vol. 109, 2004, doi: 10.1029/2003JD004457.

[6] Z. W. Li, H. F. Shen, H. F. Li, G. S. Xia, P. Gamba, and L. P. Zhang, "Multi-feature combined cloud and cloud shadows detection in GaoFen-1 wide field of view imagery," *Remote Sens. Environ.*, vol. 191, pp. 342–358, 2017.

[7] Z. Zhu and C. E. Woodcock, "Automated cloud, cloud cloud shadows, and snow detection in multitemporal Landsat data: An algorithm designed specifically for monitoring land cover change," *Remote Sens. Environ.*, vol. 152, pp. 217–234, 2014.

[8] B. Wang, A. Ono, K. Muramatsu, and N. Fujiwara, "Automated detection and removal of clouds and their cloud shadowss from Landsat TM images," *IEICE Trans. Inf. Syst.*, vol. E82D, no.2, pp. 453–460, 1999.

[9] O. Hagolle, M. Huc, D. V. Pascual, and G. Dedieu, "A multi-temporal method for cloud detection, applied to FORMOSAT-2, VENμS, LANDSAT and SENTINEL-2 images," *Remote Sens. Environ.*, vol. 114, pp. 1747–1755, 2010.

[10] J. H. Bian, A. N. Li, H. A. Jin, W. Zhao, G. B. Lei, and C. Q. Huang, "Multi-temporal cloud and snow detection algorithm for the HJ-1A/B CCD imagery of China," in *Proc. IEEE Int. Geosci. Remote Sens. Symp.*, 2014, pp. 501–504.

[11] N. R. Goodwin, L. J. Collett, R. J. Denham, N. Flood, and D. Tindall, "Cloud and cloud shadows screening across Queenland, Australia: An automated method for Landsat TM/ETM plus time series," *Remote Sens. Environ.*, vol. 134, pp. 50–65, 2013.
[12] G. Mateo-Garcia, L. Gomez-Chova, J. Amoros-Lopez, J. Munoz-Mari, and G. Camps-Valls, "Multitemporal cloud masking in the Google earth engine," *Remote Sens.*, vol. 10, no. 7, 2018, Art. no. 1079.
[13] X. L. Zhu and E. H. Helmer, "An automatic method for screening clouds and cloud shadows in optical satellite image time series in cloudy regions," *Remote Sens. Environ.*, vol. 214, pp. 135–153, 2018.
[14] S. M. Jin *et al.*, "Automated cloud and cloud shadows detection and filling using two-date Landsat imagery in the USA," *Int. J. Remote Sens.*, vol. 34, no. 5, pp. 1540–1560, 2013.
[15] C. H. Lin, B. Y. Lin, K. Y. Lee, and Y. C. Chen, "Radiometric normalization and cloud detection of optical satellite images using invariant pixels," *ISPRS J. Photogrammetry Remote Sens.*, vol. 106, pp. 107–117, 2015.
[16] R. R. Irish, "Landsat 7 science data users handbook. National Aeronautics and Space Administration," 2000, doi: 10.3133/7000070.
[17] Y. Zhang, B. Guindon, and J. Cihlar "An image transform to characterize and compensate for spatial variations in thin cloud contamination of Landsat images," *Remote Sens. Environ.*, vol. 82, no. 2–3, pp. 173–187, 2002.
[18] S. L. Chen, X. H. Chen, J. Chen, P. F. Jia, X. Cao, and C. Y. Liu, "An iterative haze optimized transformation for automatic cloud/haze detection of Landsat imagery," *IEEE Trans. Geosci. Remote Sens.*, vol. 54, no. 5, pp. 2682–2694, May 2016.
[19] S. L. Chen *et al.*, "A novel cloud removal method based on IHOT and the cloud trajectories for Landsat imagery," *Remote Sens.*, vol. 10, 2018, Art. no. 1040.
[20] Z. Zhu, S. X. Wang, and C. E. Woodcock, "Improvement and expansion of the Fmask algorithm: Cloud, cloud shadow, and snow detection for Landsats 4–7, 8, and Sentinel 2 images," *Remote Sens. Environ.*, vol. 159, pp. 269–277, 2015.
[21] S. Qiu, B. B. He, Z. Zhu, Z. M. Liao, and X. W. Quan, "Improving Fmask cloud and cloud shadow detection in mountainous area for Landsats 4–8 images," *Remote Sens. Environ.*, vol. 199, pp. 107–119, 2017.
[22] S. Qiu, Z. Zhu, and B. B. He, "Fmask 4.0: Improved cloud and cloud shadow detection in Landsats 4–8 and Sentinel-2 imagery," *Remote Sens. Environ.*, vol. 231, 2019, Art. no. 111205.
[23] L. Sun, X. T. Mi, J. Wei, J. Wang, X. P. Tian, H. Y. Yu, and P. Gan, "A cloud detection algorithm-generating method for remote sensing data at visible to short-wave infrared wavelengths," *ISPRS J. Photogrammetry Remote Sens.*, vol. 124, pp. 70–88, 2017.
[24] H. Zhai, H. Y. Zhang, L. P. Zhang, and P. X. Li, "Cloud/cloud shadows detection based on spectral indices for multi/hyperspectral optical remote sensing imagery," *ISPRS J. Photogrammetry Remote Sens.*, vol. 144, pp. 235–253, 2018.
[25] M. J. Hughes and D. J. Hayes, "Automated detection of cloud and cloud shadows in single-date landsat imagery using neural networks and spatial post-processing," *Remote Sens.*, vol. 6, no. 6, pp. 4907–4926, 2014.
[26] D. Chai, S. Newsam, H. K. K. Zhang, Y. Qiu, and J. F. Huang, "Cloud and cloud shadows detection in Landsat imagery based on deep convolutional neural networks," *Remote Sens. Environ.*, vol. 225, pp. 307–316, 2019.
[27] S. L. Hegarat-Mascle and C. Andre, "Use of Markov random fields for automatic cloud/cloud shadows detection on high resolution optical images," *ISPRS J. Photogrammetry Remote Sens.*, vol. 64, pp. 351–366, 2009.
[28] P. F. Li, L. M. Dong, H. C. Xiao, and M. L. Xu, "A cloud image detection method based on SVM vector machine," *Neurocomputing*, vol. 169, pp. 34–42, 2015.
[29] T. Bai, D. R. Li, K. M. Sun, Y. P. Chen, and W. Z. Li, "Cloud detection for high-resolution satellite imagery using machine learning and multi-feature fusion," *Remote Sens.*, vol. 8, 2016, Art. no. 715.
[30] Z. F. Shao, J. Deng, L. Wang, Y. W. Fan, N. S. Sumari, and Q. M. Cheng, "Fuzzy autoencode based cloud detection for remote sensing imagery," *Remote Sens.*, vol. 9, 2017, Art. no. 311.
[31] H. Ishida, Y. Oishi, K. Morita, K. Moriwaki, and T. Y. Nakajima, "Development of a support vector machine based cloud detection method for MODIS with the adjustability to various conditions," *Remote Sens. Environ.*, vol. 205, pp. 390–407, 2018.
[32] X. D. Kang, G. H. Gao, Q. B. Hao, and S. T. Li, "A coarse-to-fine method for cloud detection in remote sensing images," *IEEE Geosci. Remote Sens. Lett.*, vol. 16, no. 1, pp. 110–114, 2019.
[33] L. Sun, X. Y. Liu, Y. K. Yang, T. T. Chen, Q. Wang, and X. Y. Zhou, "A cloud shadows detection method combined with cloud height iteration and spectral analysis for Landsat 8 OLI data," *ISPRS J. Photogrammetry Remote Sens.*, vol. 138, pp. 193–207, 2018.
[34] P. L. Scaramuzza, M. A. Bouchard, and J. L. Dwyer, "Development of the Landsat data continuity mission cloud-cover assessment algorithms," *IEEE Trans. Geosci. Remote Sens.*, vol. 50, no. 4, pp. 1140–1154, Apr. 2012.
[35] S. Foga, *et al.*, "Cloud detection algorithm comparison and validation for operational Landsat data products," *Remote Sens. Environ.*, vol. 194, pp. 379–390, 2017.
[36] U.S. Geological Survey, L7 Irish Cloud Validation Masks. U.S. Geological Survey data release, 2016, Accessed: Feb. 28, 2017.
[37] U.S. Geological Survey, L8 Biome Cloud Validation Masks. U.S. Geological Survey data release, 2016, Accessed: Feb. 28, 2017.
[38] J. C. Dunn, "A fuzzy relative of the ISODATA process and its use in detecting compact well-separated clusters," *J. Cybern*, vol. 3, pp. 32–57, 1973.
[39] D. C. Tao, X. L. Li, X. D. Wu, and S. J. Maybank, "General tensor discriminant analysis and gabor features for gait recognition," *IEEE Trans. Pattern Anal. Mach. Intell.*, vol. 29, no. 10, pp. 1700–1715, Oct. 2007.
[40] X. Y. Hu, Y. Wang, and J. Shan, "Automatic recognition of cloud images by using visual saliency features," *IEEE Geosci. Remote Sens. Lett.*, vol. 12, no. 8, pp. 1760–1764, Aug. 2015.
[41] H. Y. Cheng and C. C. Yu, "Multi-model solar irradiance prediction based on automatic cloud classification," *Energy*, vol. 91, pp. 579–587, 2015.
[42] K. M. He, J. Sun, and X. O. Tang, "Single image haze removal using dark channel prior," *IEEE Trans. Pattern Anal. Mach. Intell.*, vol. 33, no. 12, pp. 2341–2353, Dec. 2011.
[43] X. Bai, C. T. Liu, P. Ren, J. Zhou, H. J. Zhao, and Y. Su, "Object classification via feature fusion based marginalized kernels," *IEEE Geosci. Remote Sens. Lett.*, vol. 12, no. 1, pp. 8–12, Jan. 2015.
[44] B. C. Gao and Y. J. Kaufman, "Selection of the 1.375-μm MODIS channel for remote sensing of cirrus clouds and stratospheric aerosols from space," *Amer. Meteorol. Soc.*, vol. 52, pp. 4231–4237, 1995.
[45] B. C. Gao, Y. J. Kaufman, W. Han, and W. Wiscombe, "Corection of thin cirrus path radiances in the 0.4-1.0 μm spectral region using the sensitive 1.375 μm cirrus detecting channel," *J. Geophys. Res. Atmos.*, vol. 103, no. 24, pp. 32169–32176, 1998.
[46] B. C. Gao, P. Yang, W. Han, R. R. Li, and W. J. Wiscombe, "An algorithm using visible and 1.38-μm channels to retrieve cirrus cloud reflectances from aircraft and satellite data," *IEEE Trans. Geosci. Remote Sens.*, vol. 40, no. 8, pp. 1659–1668, Aug. 2002.
[47] E. Vermote and N. Saleous, *LEDAPS surface reflectance product description, Version 2.0*, 2007.
[48] P. Soille, J. Vogt, and R. Colombo, "Carving and adaptive drainage enforcement of grid digital elevation models," *Water Resour. Res.*, vol. 39, no. 12, 2003, doi: 10.1029/2002WR001879.
[49] Y. Luo, A. P. Trishchenko, and K. V. Khlopenkov, "Developing clear-sky, cloud and cloud cloud shadows mask for producing clear-sky composites at 250-meter spatial resolution for the seven MODIS land bands over Canada and North America," *Remote Sen. Environ.*, vol. 112, pp. 4167–4185, 2008.

Ping Bo received the B.E. degree and the Ph.D degree in remote sensing science and technology in School of Remote Sensing and Information Engineering, Wuhan University, Wuhan, China, in 2009 and 2015, respectively.

In 2013, he worked at the University of Rhode Island, USA as a visiting student for one year.

His current research interests include information extraction based on satellite data and satellite-derived data recovery.

Su Fenzhen received the B.E. degree in remote sensing science and technology in School of Remote Sensing and Information Engineering, Wuhan University, Wuhan, China, in 1994, and the Ph.D. degree in State Key Laboratory of Resources and Environmental Information System, Institute of Geographic Sciences and Natural Resources Research, Chinese Academy of Sciences.

His current research interests include spatio-temporal ocean information detection, oil spilling detection, and Ocean GIS model research.

Meng Yunshan received the B.E. degree in Geomatics Engineering from Changchun Institute of Technology, Changchun, China, in 2009, the M.Sc. degree from Wuhan University, Wuhan, China, in 2011, and the Ph.D degree in State Key Laboratory of Resources and Environmental Information System, Institute of Geographic Sciences and Natural Resources Research, Chinese Academy of Sciences in 2016.

Her current research interests include high- resolution remote sensing image segmentation and geological disaster identification and monitoring using remote sensing technology.